

# Supplemental Information for Strong modulation of carrier effective mass in WTe<sub>2</sub> via coherent lattice manipulation

Davide Soranzio,<sup>1,2,\*</sup> Matteo Savoini,<sup>1</sup> Paul Beaud,<sup>3</sup> Federico Cilento,<sup>2,4</sup> Larissa Boie,<sup>1</sup> Janine Dössegger,<sup>1</sup>  
Vladimir Ovuka,<sup>1</sup> Sarah Houver,<sup>1,5</sup> Mathias Sander,<sup>3</sup> Serhane Zerdane,<sup>3</sup> Elsa Abreu,<sup>1</sup> Yunpei Deng,<sup>3</sup> Roman  
Mankowsky,<sup>3</sup> Henrik T. Lemke,<sup>3</sup> Fulvio Parmigiani,<sup>2,4,6</sup> Maria Peressi,<sup>2</sup> and Steven L. Johnson<sup>1,7,†</sup>

<sup>1</sup>*Institute for Quantum Electronics, Eidgenössische Technische Hochschule (ETH) Zürich, CH-8093 Zurich, Switzerland*

<sup>2</sup>*Dipartimento di Fisica, Università degli Studi di Trieste, 34127 Trieste, Italy*

<sup>3</sup>*SwissFEL, Paul Scherrer Institut, 5232 Villigen PSI, Switzerland*

<sup>4</sup>*Elettra-Sincrotrone Trieste S.C.p.A., 34149 Basovizza, Italy*

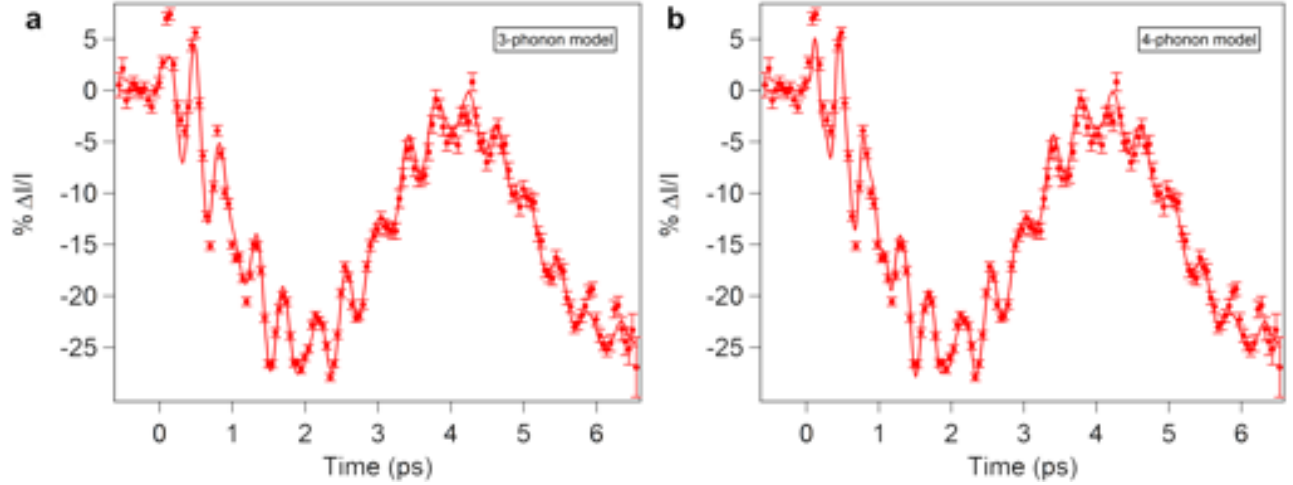
<sup>5</sup>*Université de Paris, CNRS, Laboratoire Matériaux et Phénomènes Quantiques, 75013 Paris, France*

<sup>6</sup>*International Faculty, University of Cologne, Albertus-Magnus-Platz, 50923 Cologne, Germany*

<sup>7</sup>*Paul Scherrer Institut (PSI), 5232 Villigen, Switzerland*

## SUPPLEMENTARY NOTE 1

In order to select how many oscillatory contributions should be considered in the fit expression (Eq. 1, main text), the following criterion was chosen: for datasets with a 0.5-ps time step, a single damped cosine wave was included while for traces with 0.05-ps time step a three- or four-phonon model was adopted. In this last case, a four-phonon model does not clearly improve the fit unless the data signal-to-noise ratio is very high. An example is given for the data from Fig. 1d, in the main text, as shown in Supplementary Figure 1. Nevertheless, the resulting fit parameters are very close, e.g.  $C_{2.4} = 5.3 \pm 0.4\% \Delta I/I$  and  $\tau_{2.4} = 4.8 \pm 0.9$  ps for the three-phonon model and  $C_{2.4} = 5.4 \pm 0.4\% \Delta I/I$  and  $\tau_{2.4} = 4.6 \pm 0.8$  ps for the four-phonon model.



**Supplementary Figure 1. Three- vs four-phonon models.** Comparison between the **a** three-phonon and **b** four-phonon models for peak (163). The error bars represent one standard deviation uncertainty.

As an alternative to the empirical fits to Eq. 1 (main text), it is also possible to attempt to fit the x-ray diffraction data directly to an analytical model of displacive excitation [1]. The phonon amplitude is proportional to the normal mode coordinate

$$Q(t) = \frac{\omega_0^2 k \rho \varepsilon_{\text{pump}}}{\omega_0^2 + \beta^2 - 2\gamma\beta} \int_0^\infty g(t - \tau) \left[ e^{-\beta\tau} + e^{-\gamma\tau} \left( \cos(\Omega\tau) - \frac{\beta'}{\Omega} \sin(\Omega\tau) \right) \right] d\tau \quad (1)$$

where  $\omega_0 = 2\pi f_0$  is the angular frequency,  $k$  is a proportionality constant,  $\rho$  and  $\beta$  are constants related to the rate of carrier generation and return to the ground state respectively,  $\varepsilon_{\text{pump}}$  is the fluence,  $\gamma$  is the coherent phonon damping factor,  $g$  is the temporal pump profile (chosen as Gaussian-like),  $\Omega = \sqrt{\omega_0^2 - \gamma^2}$  and  $\beta' = \beta - \gamma$ .

The coordinate  $Q(t)$  contains different contributions within the integrand. While coupled with the others through  $\beta$ , the exponentially-decaying term related to the electron relaxation which gives the initial offset to the  $\Delta I/I$  profile, while the second one is composed by oscillatory contributions giving the periodic modulations.

Its use in describing the transient x-ray intensity, however, fails when lattice thermalization and, in general, atomic reorganization occur, *e.g.* at very high fluences. It is thus only adequate close to time zero, when the cited phenomena have yet to strongly perturb the initial configuration.

If a larger time window is under study as in Fig. 1c, in the main text, one should take into account these mechanisms in the fit expression. In this example, we use a semi-empirical expression, based on a system of three coupled differential equations, to take into account the ionic dynamic disorder variation [2]

$$\begin{aligned}
2C_e \frac{\partial T_e}{\partial t} &= \frac{2(1-R)}{l_{\text{dep}}} I_L(t) - g(T_e - T_h) \\
\alpha C_1 \frac{\partial T_h}{\partial t} &= g(T_e - T_h) - g_c(T_h - T_c) \\
(1-\alpha) C_1 \frac{\partial T_c}{\partial t} &= g_c(T_h - T_c) - g_r(T_c - T_r)
\end{aligned} \tag{2}$$

where

- $C_e, C_1$  are the electronic and lattice thermal capacities;
- $T_e, T_h, T_c, T_r = 295$  K are the electronic, ‘hot’ lattice, ‘cold’ lattice and room temperatures;
- $R$  is the sample reflectivity at the pump wavelength;
- $l_{\text{dep}}$  is the pump penetration depth;
- $I_L$  is the pump intensity;
- $\alpha$  is the fraction of phonon modes efficiently-coupled to the electron system (‘hot’ lattice);  $g, g_c, g_r$  are the coupling parameters between electrons and ‘hot’ lattice, ‘hot’ and ‘cold’ lattices and ‘cold’ lattice and sample mount respectively.

Here, we treat the fraction of ‘hot’ phonons and couplings as fitting parameters.

The Debye-Waller factor, considering as first approximation an empirical average can be written as [2, 3]

$$W(G_{hkl}) = \frac{1}{2} G_{hkl}^2 \langle u^2 \rangle \tag{3}$$

where  $G_{hkl}$  is the modulus of the reciprocal lattice vector for (hkl) reflection under consideration and  $\langle u^2 \rangle$  is the isotropically-averaged mean squared displacement

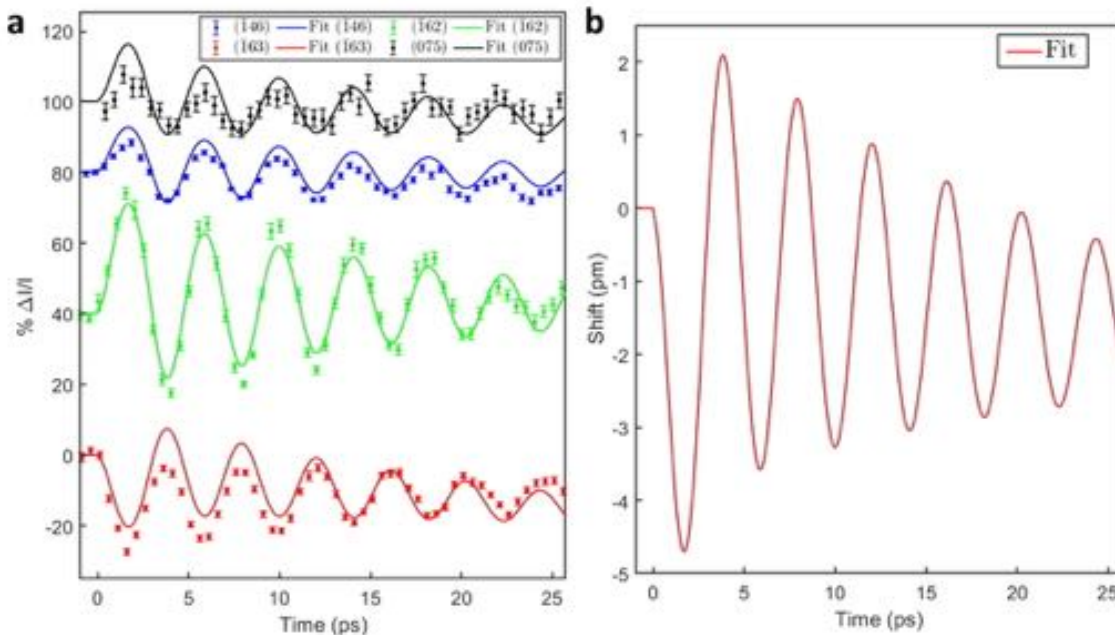
$$\langle u^2 \rangle = \frac{9\hbar^2 T_1}{M k_B \Theta_D^2} \tag{4}$$

where  $T_1$  is the effective lattice temperature  $T_1 = \alpha T_h + (1-\alpha)T_c$ ,  $M$  is the unit cell mass,  $k_B$  is the Boltzmann constant and  $\Theta_D$  is the Debye temperature.

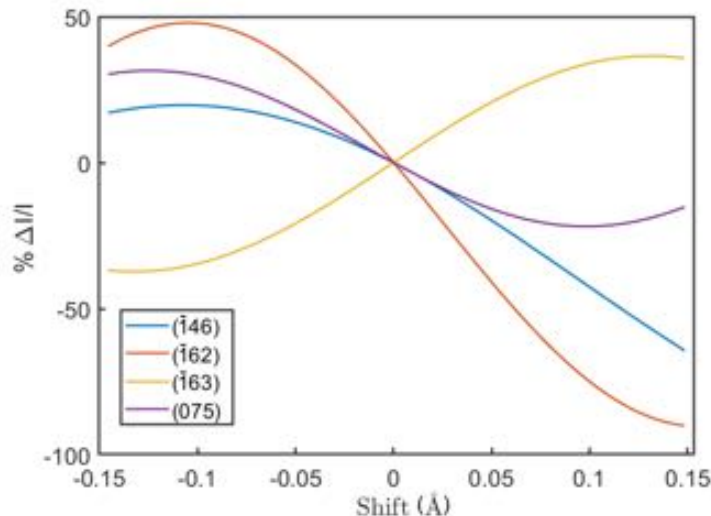
The Debye-Waller factor is then implemented in the formula for the diffracted intensity as

$$I(G_{hkl}) = I_0(G_{hkl}) \exp[-2W(G_{hkl})] \tag{5}$$

where  $I_0(G_{hkl})$  is the diffracted intensity in the  $T_1 \rightarrow 0$  K limit.



**Supplementary Figure 2. DECP model fitting in the intermediate time-range.** **a** Comparison among experimental data and their simultaneous global fit. The upper profiles and fit curves were vertically shifted for clarity. **b**  $y$ -shift of the W#1 (see Supplementary Figure 6a) position extracted from the results shown in panel a. The error bars represent one standard deviation uncertainty.



**Supplementary Figure 3. Diffraction intensity variation and shear coordinate.**  $\Delta I/I$  variation for the four examined peaks with respect to the equilibrium configuration (shift = 0) for a shift along the shear mode coordinates, referred to W#1 (see Supplementary Figures 6a, 9a), using the DFPT eigendisplacement for the shear mode.

The slow drift of the structure along the shear mode described in the ‘Additional time-resolved x-ray data’ section of this document is included by adding a  $at^b$  term to the shear normal coordinate (Eq. 1), where  $a$  and  $b$  are fit parameters and  $t$  is the time delay with respect to time zero.

A quantitative description of the thermalization process should also take into account the anisotropy of  $WTe_2$  as well as the formation of spatial temperature gradients.

While the inclusion of these corrections improves the long-delay description, there are still large discrepancies near time zero, especially for  $(\bar{1}63)$  (Supplementary Figure 2). These can be ascribed mainly to limitations of the DFT-based dispersive model as well as to the small variation in the penetration depth of the infrared pulse among the measured peaks.

In Supplementary Figure 3 we model the behavior of the relative variation of the modulus squared of the structure factor, equivalent to  $\Delta I/I$  in the model, for the various peaks. This modification is represented as a function of the position shift for atom W#1 (see Supplementary Figure 6a) when a shear displacement with respect to the equilibrium configuration occurs. This shift direction is the one along which the system is expected to evolve after the excitation, *i.e.* towards the transient  $1T'^{(*)}$  phase [4, 5].

This sliding also leads to changes in the  $\Delta I/I$  oscillation amplitude of the  $A_1$  modes, when the atoms are shifted along the shear coordinate. In Supplementary Figure 4, we show the  $\Delta I/I$  variations calculated by rigidly displacing the structure along the eigendisplacements (Supplementary Figure 9) as a function (horizontal axis) of the position shift of the atom W#1 along the shear coordinate. For the shear mode, we considered a  $\pm 2.5$  pm oscillation along  $y$  (numerical average among the atomic basis) around the initial position, while for the other  $A_1$  modes, whose frequencies are close to the Fourier transform peaks resolved in Fig. 1e (main text), we set a  $\pm 300$  fm oscillation along  $z$  (maximum value within the atomic basis).

This shows that even in the case of small mismatches in the determination of initial or gradual shifts along the shear coordinate, we still obtain a reasonable estimate for the displacements connected to the  $\Delta I/I$  oscillations. Naturally, this consideration assumes the dynamical matrix to remain almost unperturbed by these shifts [6].

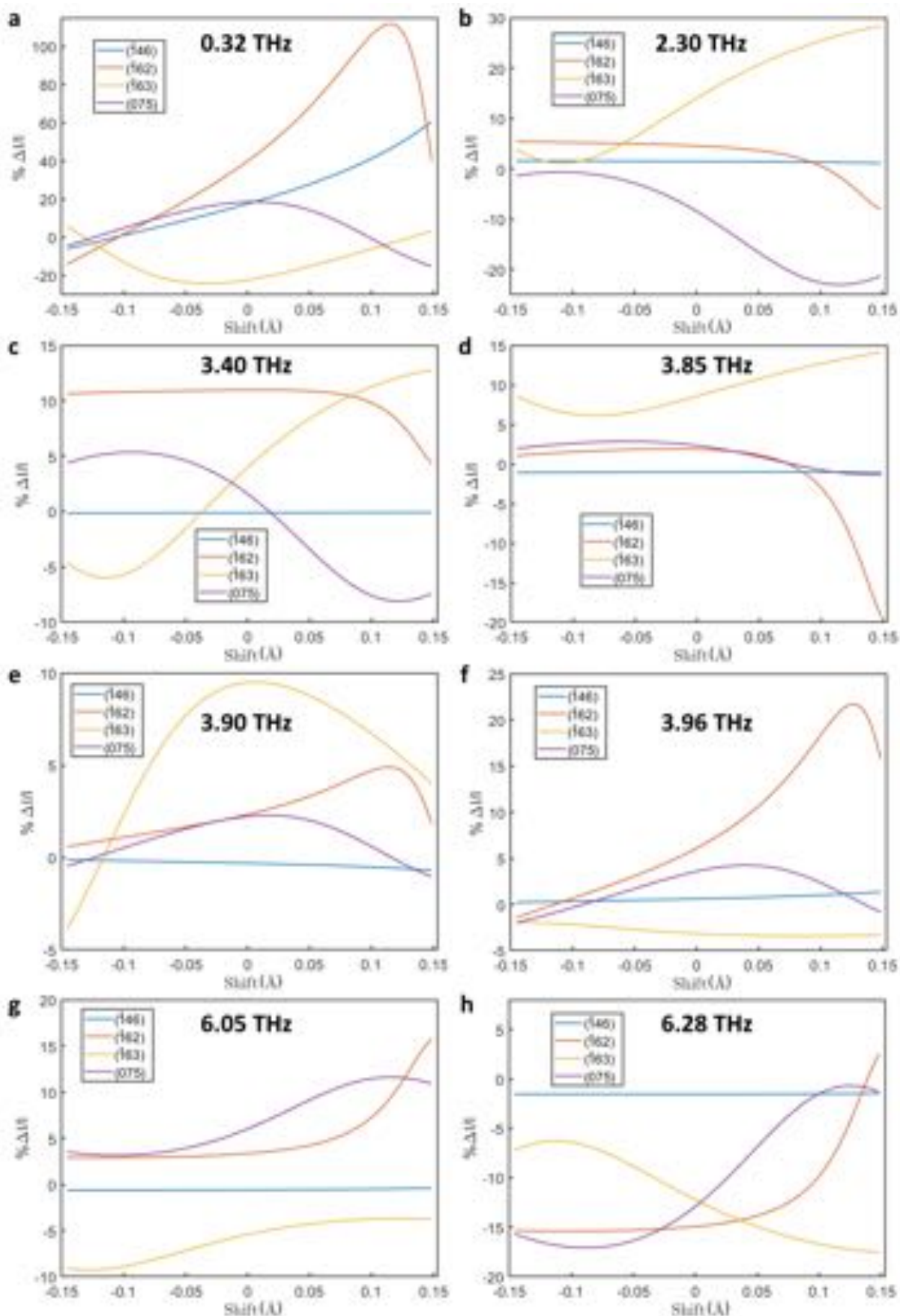
Considering the fine-sampled delay interval after time zero for  $(\bar{1}63)$ , we focused on the higher-frequency modes (Supplementary Figure 5). In order to fit the single profile, we allowed the shear mode  $\beta$  parameter (see Eq. 1) to change, in contrast to the other parameters associated to such mode from the previous fitting. This was necessary to obtain a reliable fit of the higher-frequency modes due to the presence of the initial discrepancy between data and global fit (Supplementary Figure 2a). Nonetheless, as shown in Supplementary Figure 4, the phononic effects on the  $\Delta I/I$  for  $(\bar{1}63)$  are seen to slowly vary for a few-pm shift along the shear coordinate.

While recognizing the two lower  $A_1$  modes is straightforward, the assignment of the third mode at  $\approx 3.4$  THz is more challenging. Together with the fitting results, we exploited Supplementary Figures 16, 4. From Supplementary Figure 9, we note that the phonons c-f are the ones which are the closest in frequency to the detected frequency. As shown in the experimental data in Supplementary Figure 16a, of the reflections we investigated the  $(\bar{1}63)$  is the most sensitive to displacements of the higher-frequency modes. One would expect the phonon modes d and e to be responsible for the most prominent effects at such frequency. This is motivated by the fact that, as shown in Supplementary Figure 4, the ratio amongst the phononic  $\Delta I/I$  shows a preponderant effect for  $(\bar{1}63)$ . This is supported by the fit results, where the phononic displacements are linearly combined, when studying the evolution of the system through the DECP model. Considering the first two modes (Supplementary Figures 9a,b) and one of the four possible choices for the third mode in the fit expression, we obtain that only the two modes in Supplementary Figures 9d,e give an appreciable improvement from a two-phonon fit. However, the examined peaks are not enough, due to their comparable predicted response, to separate these contributions in a possible four-phonon model.

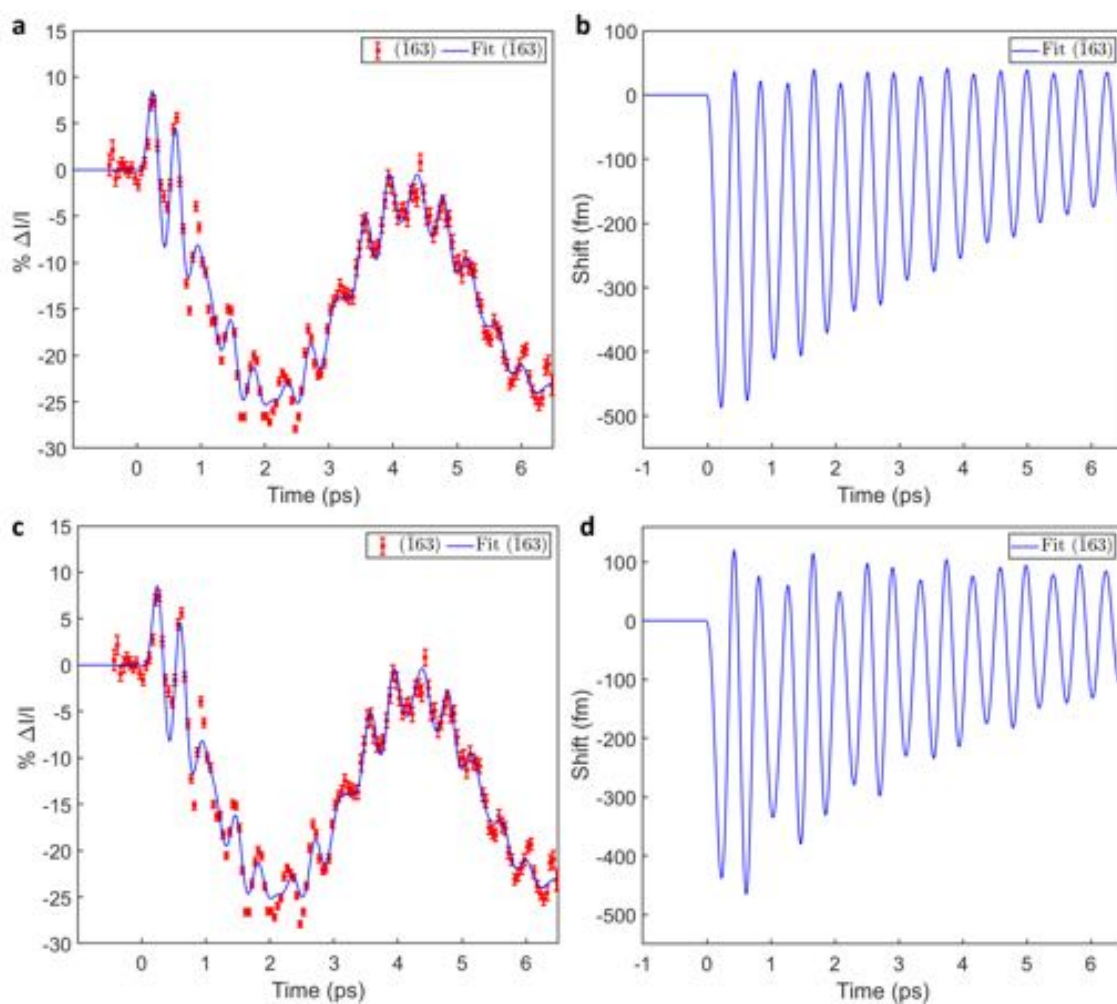
The assignment of the weak  $\approx 6.2$  THz mode identified in Fig. 1e, in the main text, is difficult because of its very low amplitude. Either of the two modes depicted in panels i and j in Supplementary Figure 9 have approximately the correct frequency.

The resulting initial displacement values are  $3.4 \pm 0.4$  pm for the shear mode and  $240 \pm 80$  fm for the 2.4 THz mode. Overall, the displacement values give compatible results with those of the empirical fit. The reason why this model was not chosen to be the primary one is connected to the high number of free parameters, especially for the thermal response, to properly account for the entire dynamics. In particular, for the shorter time scans, where the slower energy redistribution has only partially occurred, this gives a non-negligible correlation between parameters which could impact the accuracy of the results.

This issue could be mitigated by obtaining detailed thermal response parameters through a separate study taking into account the material anisotropy, which, however, is beyond the scope of this work.



**Supplementary Figure 4. Diffraction intensity variation and phonon displacements.**  $\Delta I/I$  variation for the four examined peaks calculated as symmetric peak-to-peak phonon oscillations around the corresponding position along the shear coordinate (referred to the  $y$ -shift of W#1) represented by the horizontal axis, referred to the equilibrium configuration. The set displacements are **a** 2.5 pm along  $y$  (average) **b-h** 300 fm along  $z$  (maximum value among the atoms). For the atomic labels and eigendisplacements see Supplementary Figures 6a, 9.

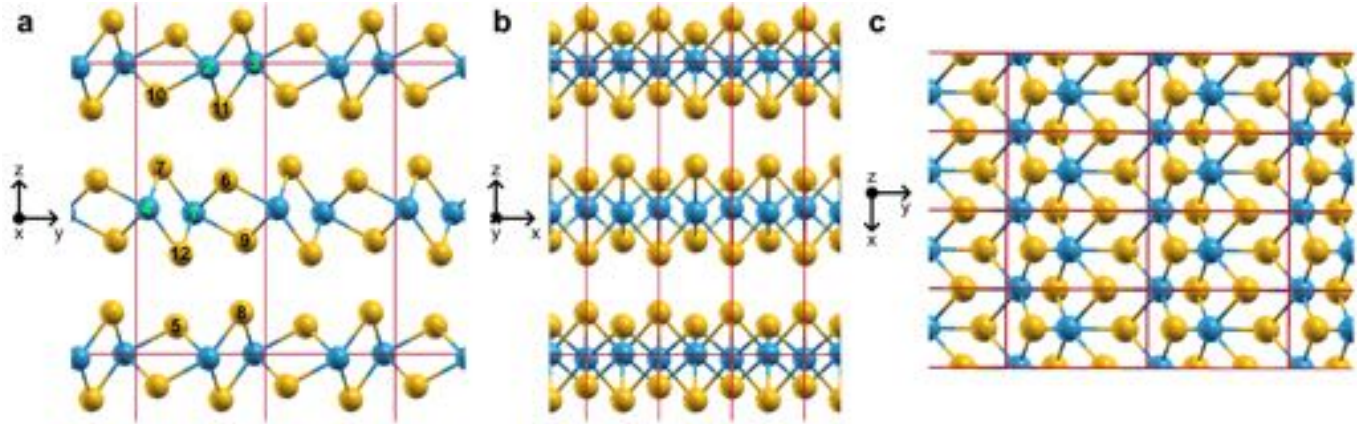


**Supplementary Figure 5. DECP model fitting of  $(\bar{1}63)$  data from Fig. 1d, in the main text. a** Experimental data and fit curve using as third phonon mode d from Supplementary Figure 9; **b**  $z$ -shift of the W#1 position extracted from the results shown in panel a; **c** Experimental data and fit curve using as third phonon mode e from Supplementary Figure 9; **d**  $z$ -shift of the W#1 position extracted from the results shown in panel c. For the atomic labels and eigendisplacements see Supplementary Figures 6a, 9. The error bars represent one standard deviation uncertainty.

## SUPPLEMENTARY NOTE 2

### Crystal structure

In Supplementary Figure 6, we report selected projections of  $\text{WTe}_2$ 's orthorhombic ( $T_d$ ) structure using XCrySDen [7]. Although an inversion center is absent among its space group elements [8], subsequent layers are almost connected by an inversion symmetry, leading to analogous characteristics, *e.g.* projected density of states, shared by more atoms than simply the Wyckoff equivalents.



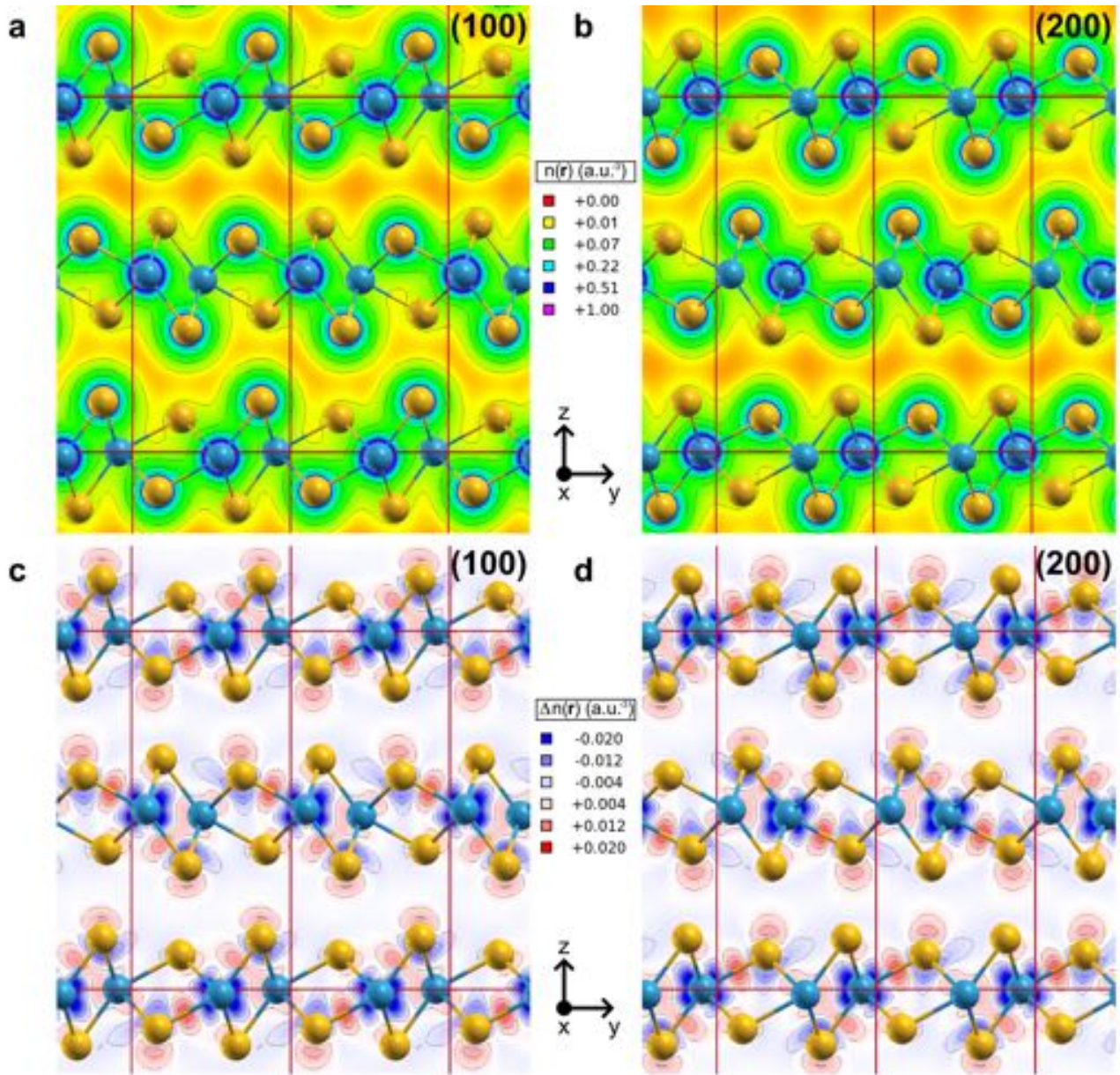
**Supplementary Figure 6. Projections of  $\text{WTe}_2$  crystal structure.** **a**  $yz$  plane, where the numerical labels for the unit-cell basis are applied for later reference **b**  $xz$  plane **c**  $xy$  plane (only one layer, the central one in panel a, is shown for clarity); the unit cell is demarcated by red lines.

The octahedral distortion is influenced by the interaction between the tungsten atoms through bonding, which has been also observed for other tungsten-based compounds [9]. This feature can be visualized through electron density surfaces (Supplementary Figures 7, 8); the charge density is plotted as numerical density in  $(\text{Bohr radius})^{-3}$ . While the charge is primarily confined close to the individual atoms (Supplementary Figures 7a,b, 8a), in-layer directional W-Te and W-W bond formation is clearly visible when we consider the difference between the electron density of the system and the sum of the single isolated atomic electronic densities (Supplementary Figures 7c,d, 8b). We observe that while the tungsten atoms all exhibit a distorted octahedral configuration, the tellurium atoms can be separated in two groups in which the electronic density close to the atoms showcases similar features. Taking as a reference Supplementary Figure 6a, we see that the Te atoms can be grouped as numbers #5, 6, 9, 10 and #7, 8, 11, 12, which constitute two different tellurium chains when observed in the  $xy$  plane (Supplementary Figure 6c).

### Equilibrium properties

The energy levels around the Fermi level are primarily connected to the in-plane bonds among tungsten 5d orbitals and tellurium 5p orbitals with varying character depending on k-point, total angular momentum and specific wavefunction [4]. Those orbitals are also the ones involved in the valence bonds. As discussed in [5], the removal of electrons close to the Fermi level could perturb these bonds and be the trigger for out-of-equilibrium evolution of the structure along the shear coordinate.

In Supplementary Table I we list the effective mass equilibrium values. We tag the different bands by a number which expresses their energy order starting from the lowest to the highest considered in the analysis. The band oscillations are presented in Supplementary Figure 12.

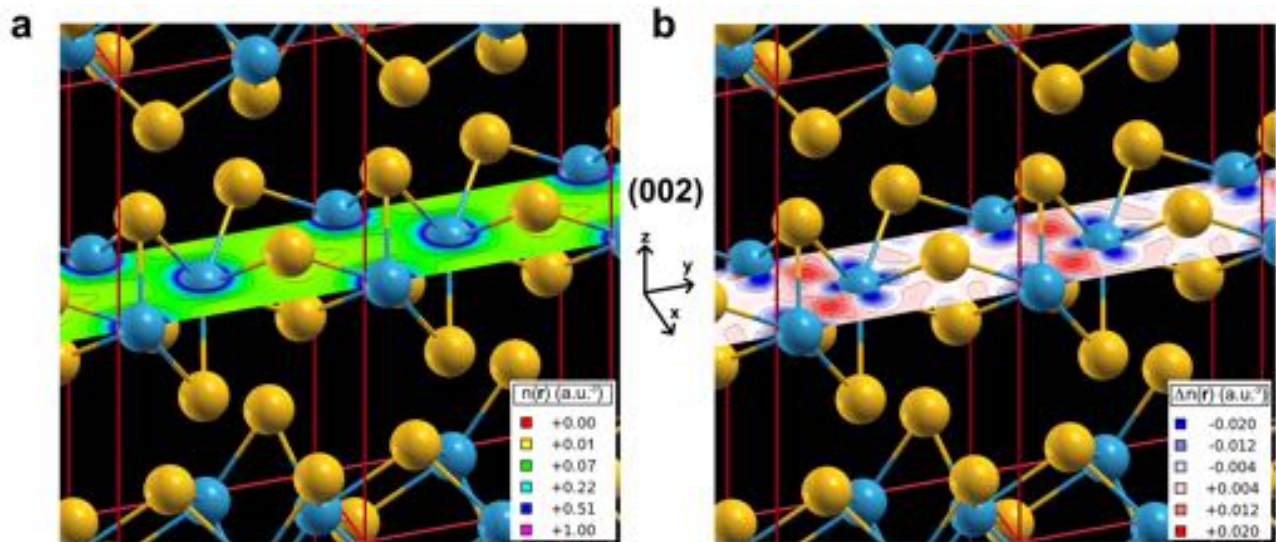


**Supplementary Figure 7. Electronic density maps perpendicular to the  $x$ -axis.** Electron density planes of  $\text{WTe}_2$  for the **a** (100) surface **b** (200) surface. Electron density differences with respect to the superposition of atomic electron density are reported for the **c** (100) surface **d** (200) surface. Black isolines are reported as a guide for the eye. The unit cell is demarcated by red lines.

Region	P1	P2	P3	P4
Effective mass	0.531 (Band 5)	0.384 (Band 5)	0.433 (Band 4)	1.653 (Band 1)
$m_{xx}^*/m_o$	0.527 (Band 6)	1.049 (Band 6)	\	0.774 (Band 2)

**Supplementary Table I.** Equilibrium effective masses  $m_{xx}^*$  at the band extrema in the regions highlighted in Fig. 5d (main text).

To obtain the zone-center phonon eigenvalues and eigenvectors, the dynamical matrix was calculated and diagonalized in a density functional perturbation theory (DFPT) [6] approach under the scalar relativistic approximation [10], a kinetic energy cutoff of 50 Rydberg and a  $8 \times 6 \times 4$  k-point mesh.



**Supplementary Figure 8. Electronic density maps perpendicular to the  $z$ -axis. **a** Electron density of  $\text{WTe}_2$  for the (002) surface. **b** Electron density difference with respect to the superposition of atomic electron densities for the (002) surface. Black isolines are reported as a guide for the eye. The unit cell is demarcated by red lines.**

The phonon eigendisplacements for the zone-center  $A_1$  modes are reported in Supplementary Figure 9 and ordered by increasing eigenvalue. All the  $A_1$  modes involve displacements in the  $yz$  plane, while no shift along the  $x$  direction is involved due to the mirror symmetry element ( $C_{2v}$  point group [8]) perpendicular to  $x$ .

### Phonon-induced strain effects on the electronic bands

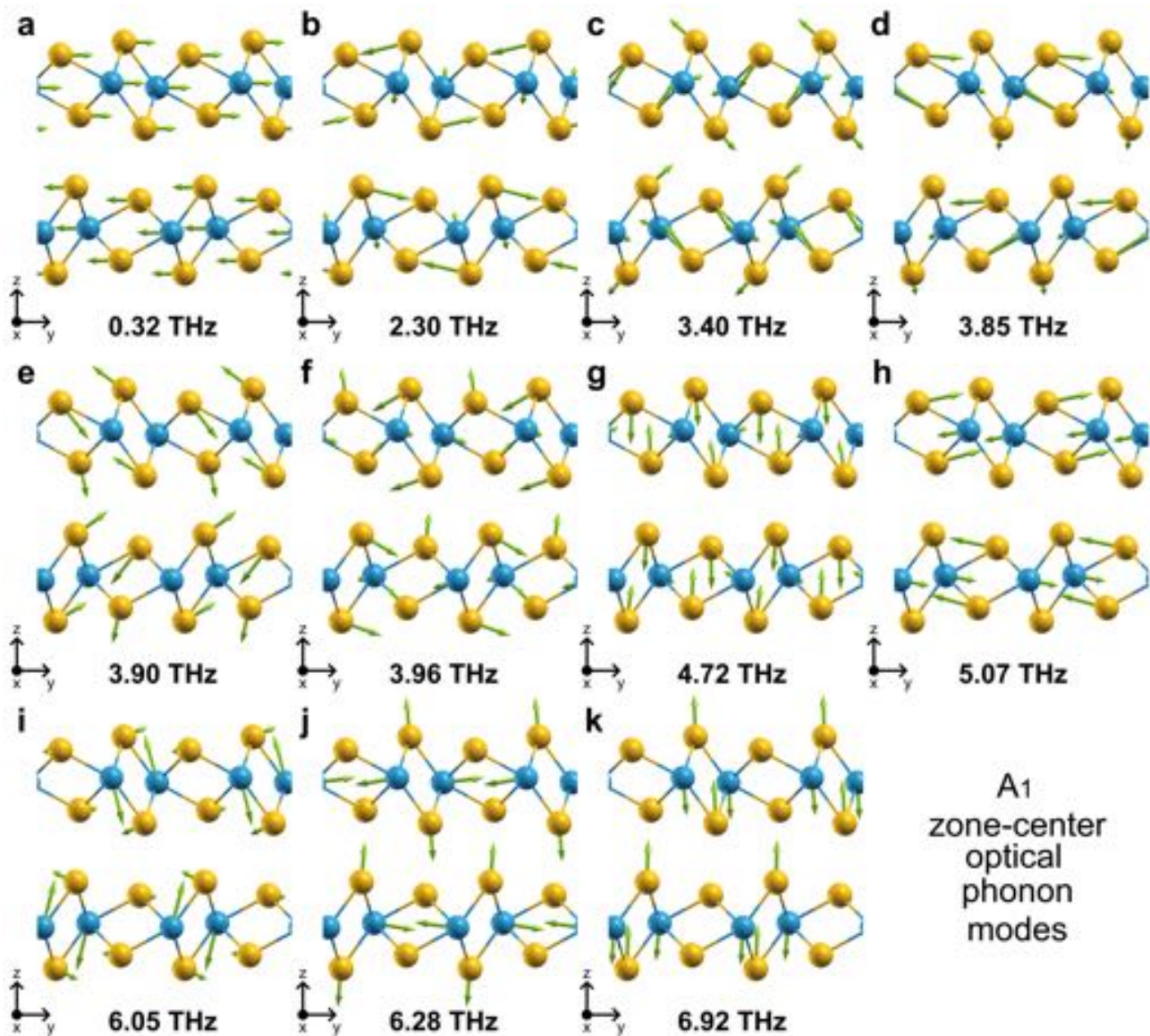
To avoid confusion, we reported in the main text the shear mode displacements in terms of the average  $y$ -coordinate shift, while the 2.4 THz modifications are presented in terms of the associated tungsten  $z$ -shift, which is  $\approx 2.44$  times smaller than the maximum  $y$ -shift for such mode. Differently from the shear mode, the 2.4 THz phonon involves non-uniform  $y$ - and  $z$ -shifts, which perturb the in-layer covalent bonds between the atoms, varying their relative distances. As the displacements are increased, the effects become more asymmetric between + and - variations, which also suggests the failure of a symmetric potential picture.

As discussed in the main text, displacing the structure along the phonon eigendisplacements leads to a quasi-symmetric modulation of the bands, which is not simply a uniform energy shift, but it also leads to a change in the band curvature. Around the regions of interest marked in Fig. 5c (main text), the bands along the  $\hat{k}_x$  direction wiggle as shown in Supplementary Figure 12. However, while the band extremum remains close to the equilibrium position for the P1 region, this does not apply for most of the other investigated cases. This is relevant if one wants to obtain the band curvature at other  $k$ -paths passing through a specific band extremum.

The effective mass tensor components obtained around the investigated regions using  $\hat{k}_y$  and  $\hat{k}_z$  dispersions are generally much larger than the ones solely involving the  $\hat{k}_x$  direction. At equilibrium (Supplementary Figure 13),  $m_{yy}$  has the following values: 3.55  $m_0$  and 3.46  $m_0$  at P1 for bands 5 and 6; 2.09  $m_0$  and 2.23  $m_0$  at P2 for bands 5 and 6; 0.62  $m_0$  at P3 for band 4; 1.82  $m_0$  and 1.44  $m_0$  at P4 for bands 1 and 2. For  $m_{zz}$  the dispersion is even flatter giving 26.60  $m_0$  and 16.26  $m_0$  at P1 for bands 5 and 6 and 9.79  $m_0$  at P3 for band 4.

The detailed shape of the bands can be influenced by electron correlation effects, which we can approximate to different levels. In the following, we report the tests performed using the DFT+U approach, as implemented in QUANTUM ESPRESSO [11, 12] using a  $U=2$  eV correction for tungsten, as in [13], as an example. All the other technical parameters of the calculations were left unchanged.

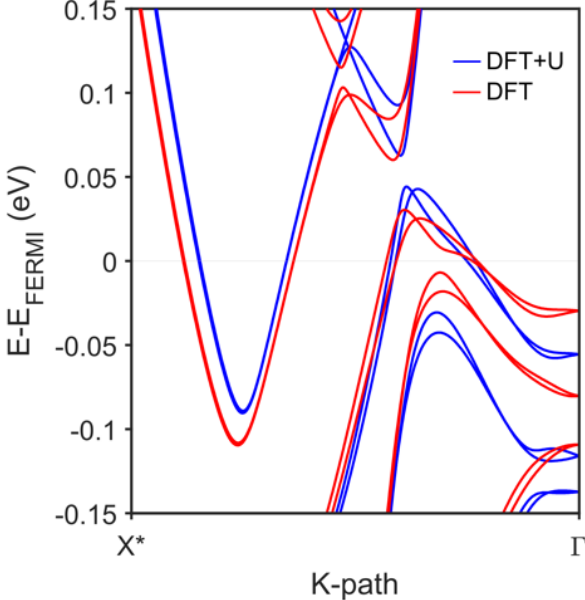
In Supplementary Figure 10, we report a comparison between the band dispersion along  $X^* (0.3 \ 0 \ 0) - \Gamma (0 \ 0 \ 0)$  around the Fermi level with and without the Hubbard correction. Most of the general characteristics are retained



**Supplementary Figure 9. Zone-center  $A_1$  optical phonons for  $WTe_2$ .** Eigendisplacements resulting from the DFPT calculations.

especially regarding the band shapes and crossing. Furthermore, while the specific effective masses are different, the percentage changes are very similar as shown in Supplementary Figure 11. The largest differences are found in the region P3 where two bands of the hole pocket intersect. The labels of the regions in reciprocal space are the same ones used in Fig. 5d in the main text.

A very accurate detailed room-temperature experimental study of the band structure would help to identify the best theoretical approach, which parameters must be changed or whether many-body effects have to be included. Nevertheless, due to the experimental broadening of these features, it is a challenging task.



**Supplementary Figure 10. DFT+U vs DFT electronic bands.** Comparison between the band dispersion obtained with and without the Hubbard correction  $U=2$  eV.

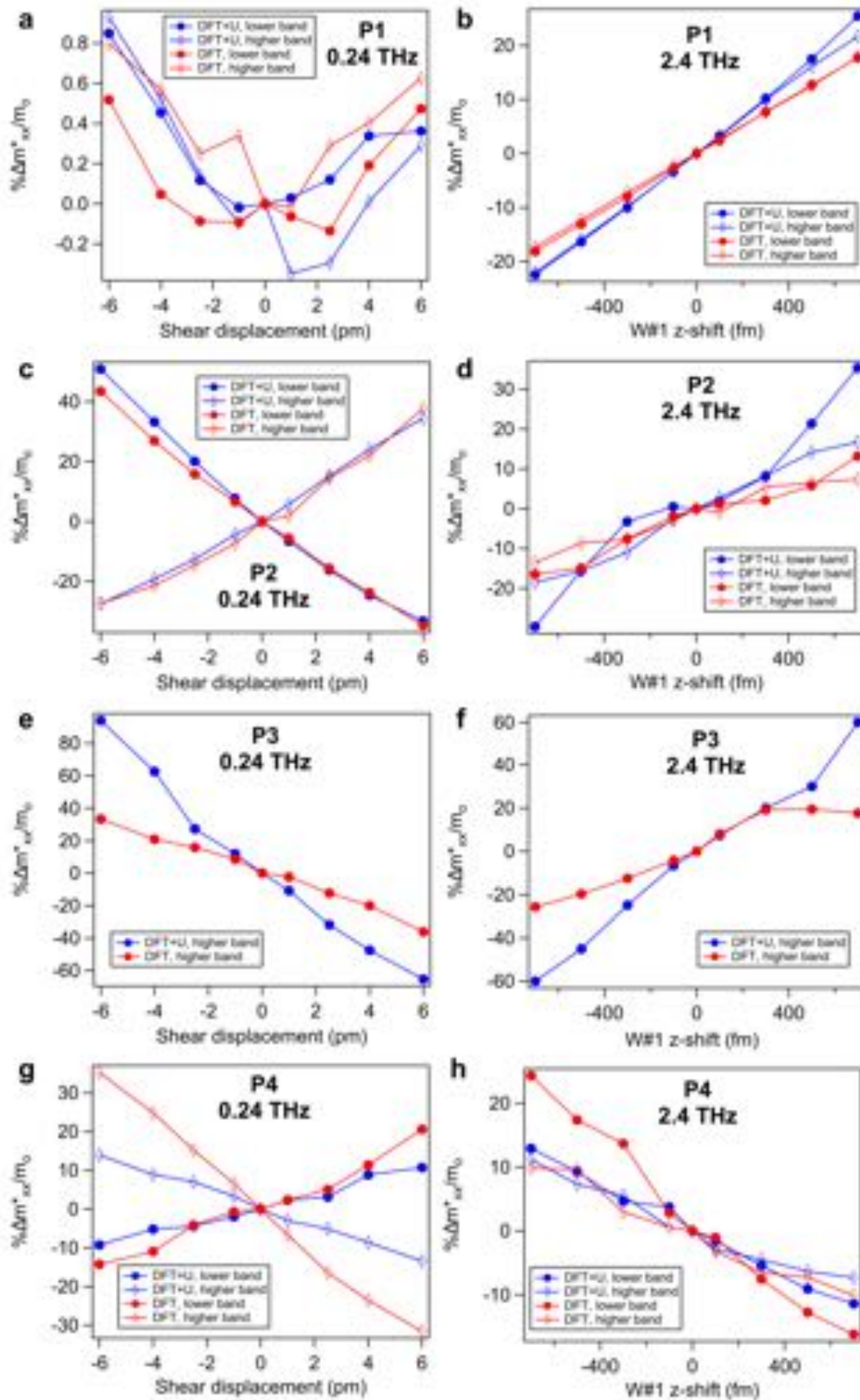
In Supplementary Figure 14, we show the Helmholtz free energy per unit cell (at  $T = 0$  K) as a function of a uniform shear shift from equilibrium, resembling the 0.24 THz (DFT: 0.32 THz) shear mode displacement and the largest  $y$ -shift for the 2.4 THz (DFT: 2.30 THz) mode. For the first curve, the horizontal axis is referred to the W#1 displacement, considered positive for the direction shown in Supplementary Figure 9a. The second curve follows the Te#7 shift, which presents the largest  $y$ -displacement for that mode and is regarded as positive when it follows the direction displayed in Supplementary Figure 9b. The atom labeling can be found in Supplementary Figure 6a. The first curve presents a clear asymmetry in the investigated range around the DFT-relaxed configuration obtained through QUANTUM ESPRESSO [11] with a second minimum for the free energy along the shear coordinate. A similar result is presented in Ref. [5], where the intermediate  $1T'(^*)$  phase is found in the direction of a second minimum of the curve. This is true in this work as well, where the  $1T'(^*)$  phase is reached for negative W#1 displacements.

The curvature and slope of the lower frequency mode between the two minima in Supplementary Figure 14 depend on the pseudopotential used, as shown in [5], although with comparable energy differences. This variability is understandable when looking at the energy scale: we are here treating differences that are fractions of 1 meV.

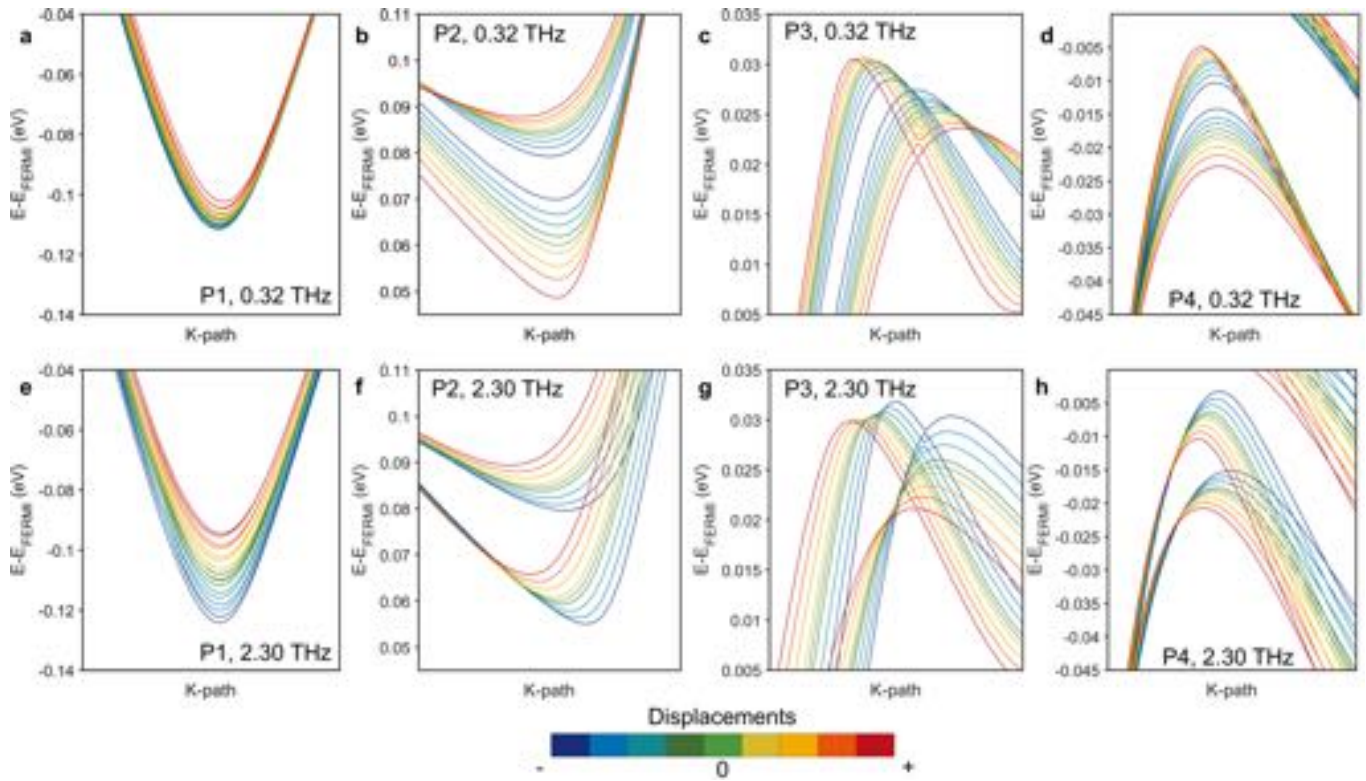
In 15 the parabolic fit for the 2.4 THz optical mode results is reported, showing a close correspondence to a parabolic dispersion. Comparing similar displacements moduli, one obtains that the energy differences with respect to the equilibrium are several times larger than for the shear mode.

In other words, the second derivative of the free energy with respect to the atomic displacement is much higher for the 2.4 THz mode. This is connected to the more severe impact on the electronic charge distribution for such mode. This is clearly seen when comparing Supplementary Figures 7c,d and 8b with the eigendisplacements of the two modes in Figs. 9a,b. The 2.4 THz mode perturbs the shared charge in covalent bonds, while the 0.24 THz mode has a minor impact on those regions.

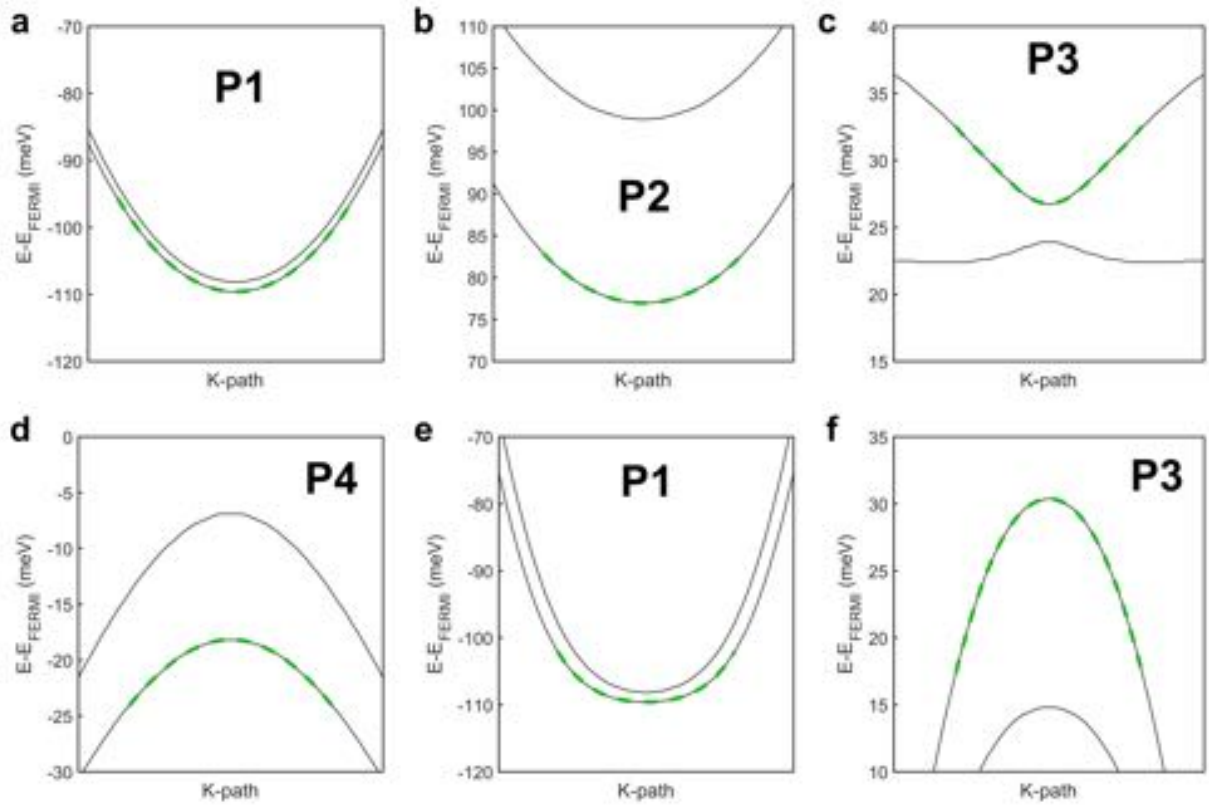
For a quantitative description of the curves at room temperature, one should consider  $T \neq 0$  K kinetic energy and entropy contributions to the free energy.



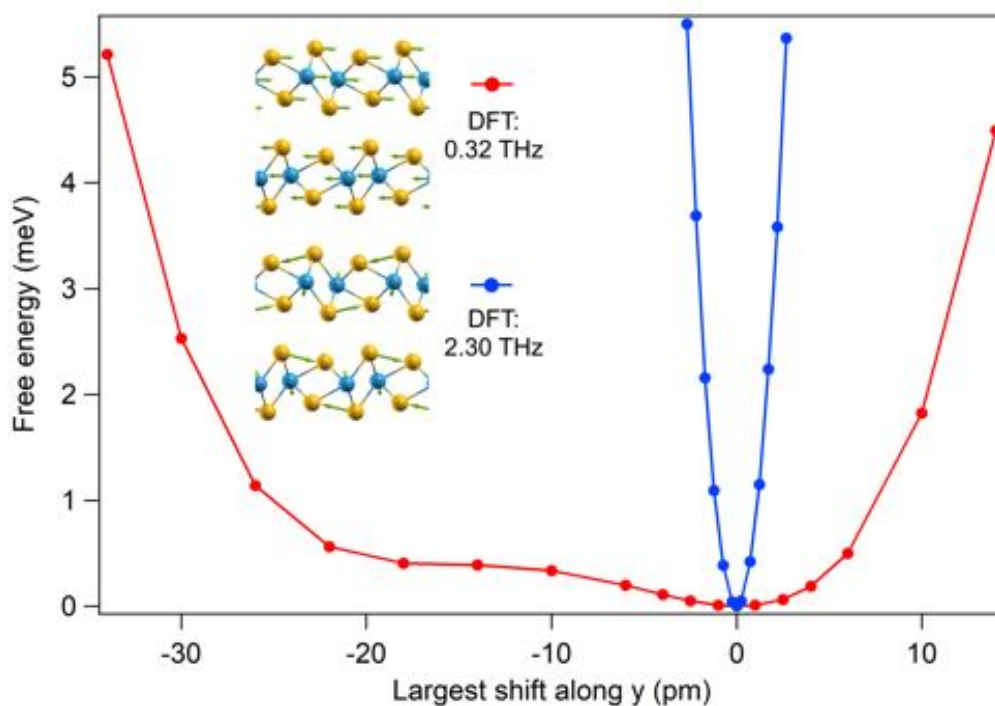
**Supplementary Figure 11. DFT+U vs DFT effective masses.** Comparison between the effective masses variations in selected reciprocal space regions for two  $A_1$  mode displacements with and without the Hubbard correction on tungsten. Their location can be found in Fig. 5d (main text) and in the associated caption. The frequency labels are the same (experimental) as the ones used in Fig. 5d (main text) for consistency.



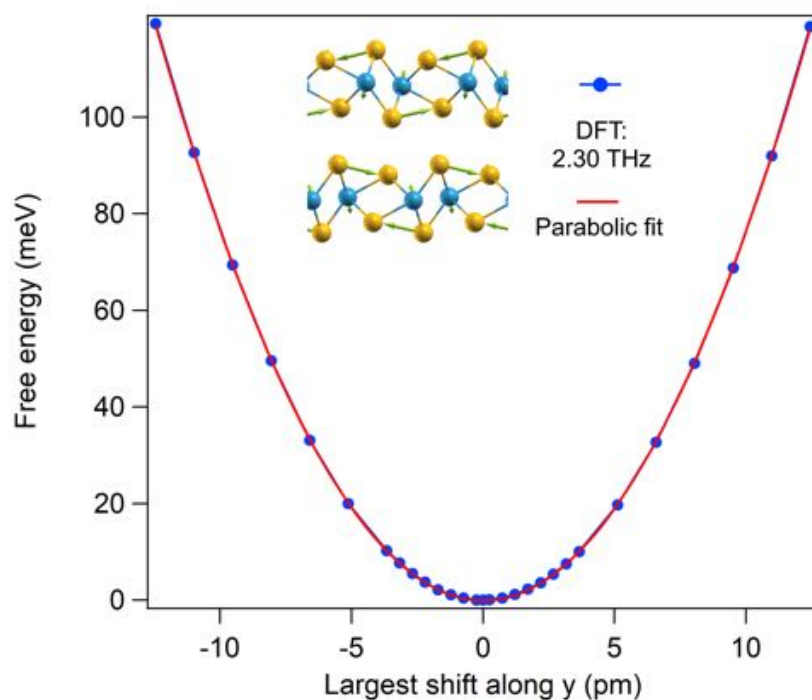
**Supplementary Figure 12. Band modifications while displacing the structure along the phonon eigendisplacements.** The displacements are considered positive when they follow the same directions as in Supplementary Figure 9. Band dispersions along the  $\hat{k}_x$  direction around the P1 (0.228 0 0), P2 (0.123 0 0), P3 (0.117 0 0), P4 (0.093 0 0) k points for the **a-d** 1<sup>st</sup>  $A_1$  mode ( $\approx 0.24$  THz) and **e-h** 2<sup>nd</sup>  $A_1$  mode ( $\approx 2.4$  THz) phonon effects. The various displacements correspond to the data points reported in Supplementary Figures 5f-i. The coordinates are expressed in reciprocal lattice units.



**Supplementary Figure 13. Band dispersions along the other reciprocal axes.** Along  $\hat{k}_y$  around **a** P1 (0.228 0 0) **b** P2 (0.123 0 0) **c** P3 (0.117 0 0) **d** P4 (0.093 0 0) and  $\hat{k}_z$  around **e** P1 (0.228 0 0) **f** P3 (0.117 0 0). The dotted green curves are examples of the fit curves employed to derive the effective masses close to the band extrema. The coordinates are expressed in reciprocal lattice units.



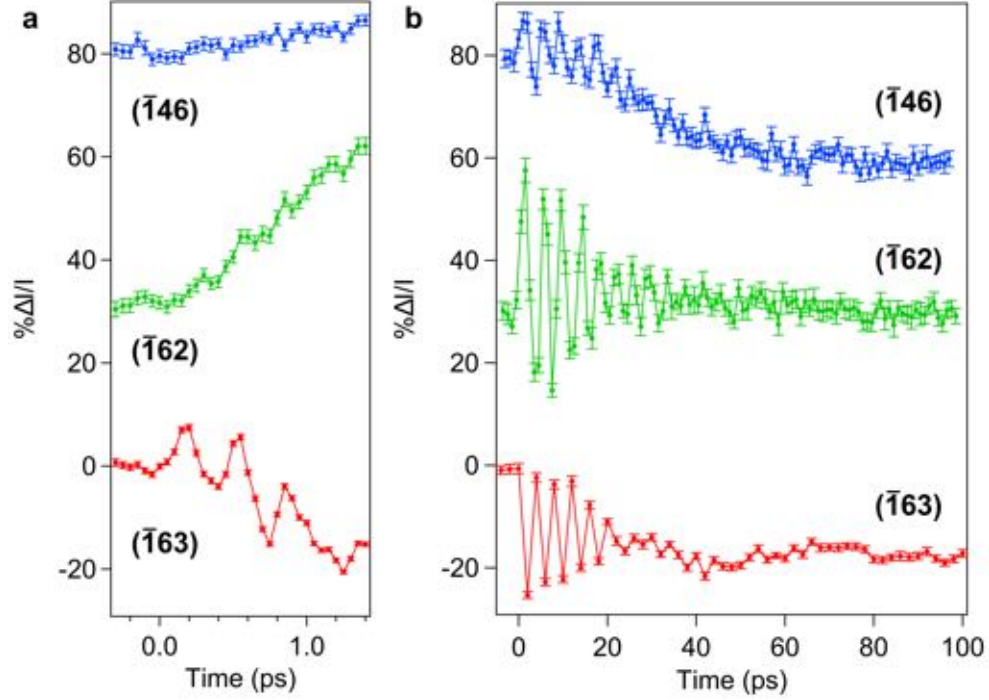
**Supplementary Figure 14. Free energy dependency on the phonon mode and amplitude.** Comparison of the Helmholtz free energy variations at  $T = 0$  K, as a function of a uniform shear shift from equilibrium, positive when referred to W#1 direction shown in Supplementary Figure 9a, resembling the 0.24 THz (DFT: 0.32 THz) mode and the largest  $y$ -shift for the 2.4 THz (DFT: 2.30 THz) mode, considering positive the Te#7 direction displayed in Supplementary Figure 9b. See Supplementary Figure 6a for the atom labeling.



**Supplementary Figure 15. Free energy variation based on the 2.4 THz mode amplitude.** Helmholtz free energy variations at  $T = 0$  K, as a function of the largest  $y$ -shift for the 2.4 THz (DFT: 2.30 THz) mode. The horizontal axis follows the  $y$ -axis Te#7 displacement (see Supplementary Figure 6a), considering positive its direction displayed in Supplementary Figure 9b. The parabolic fit curve shows a very close accordance with the simulated data.

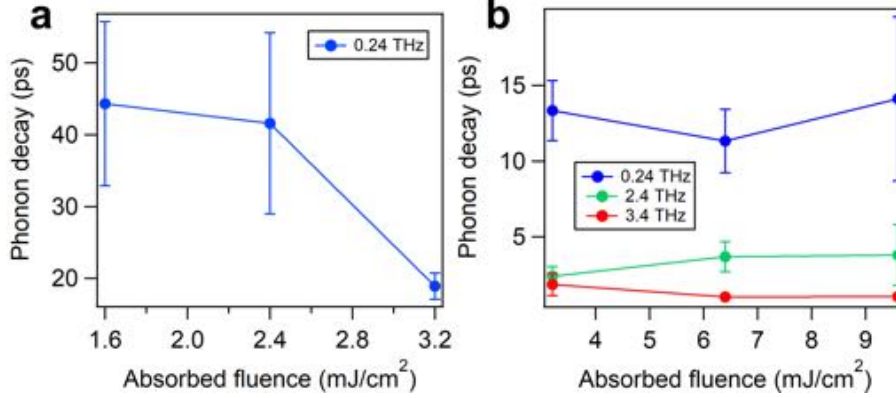
## SUPPLEMENTARY NOTE 3

In Supplementary Figure 16, we report the diffracted intensity dynamics for the  $(\bar{1}46)$ ,  $(\bar{1}62)$  and  $(\bar{1}63)$  reflections acquired using different time steps over additional time windows with respect to the main text (Fig. 1). Panel a shows the different impact of the high-frequency content in the first few hundreds of femtoseconds, while panel b presents, together with the shear mode oscillations in the first 30 ps, a slower  $\Delta I/I$  variation which is connected to lattice heating and, possibly, a shift of the structure along the shear coordinate as discussed in the main text and later on in this section.



**Supplementary Figure 16. Supplemental x-ray time profiles.**  $\Delta I/I$  profiles for the  $(\bar{1}46)$ ,  $(\bar{1}62)$ ,  $(\bar{1}63)$  Bragg reflections **a** around time zero and **b** in an extended time window taken at room temperature and  $3.2 \text{ mJ/cm}^2$  absorbed fluence. The traces have been shifted for clarity. The error bars represent one standard deviation uncertainty.

In Supplementary Figure 17, we report the fluence dependence of the time-decay constants from the fits to the data of Figs. 2a, 3a,b to Eq. 1 (main text). At lower fluences the uncertainty is large since the time-decay constants are much longer than the reported time windows [14].



**Supplementary Figure 17. Fluence dependence of the phonon time-decay constants.** **a** ( $\bar{146}$ ) (from Fig. 2a, in the main text), one-phonon model **b** ( $\bar{163}$ ) (from Figs. 3a,b in the main text), three-phonon model. The error bars represent one standard deviation uncertainty.

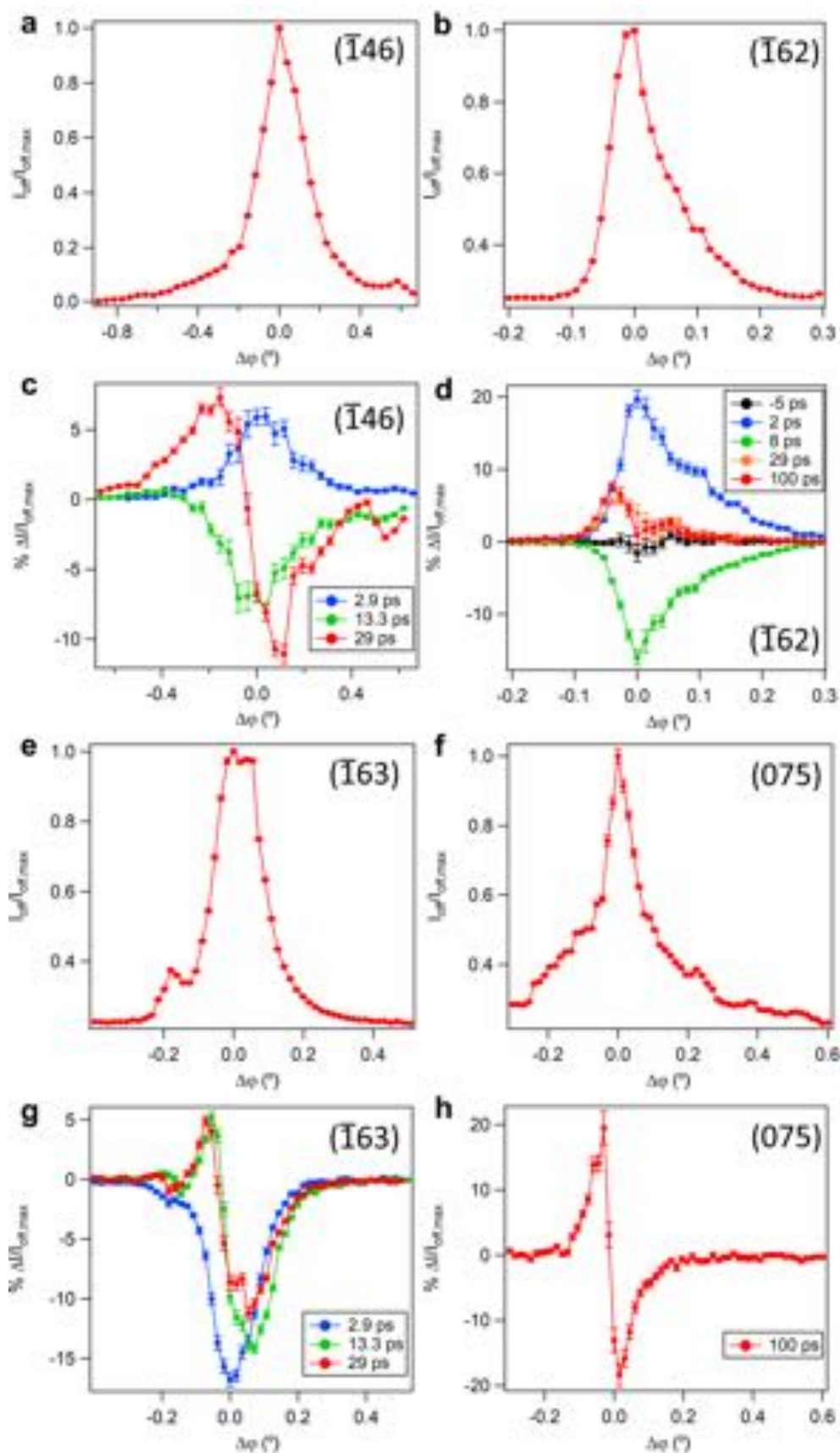
Regarding the initial phases of the modes, using our empirical model (Eq. 1 in the main text), we obtain, as fit parameters, an initial phase  $\phi_1 = -91 \pm 6$  degrees for the shear mode (average result considering the traces in Fig. 1c, from the main text and taking into account of the sign inversion for ( $\bar{163}$ )) and  $\phi_2 = -36 \pm 4$  degrees for the 2.4 THz mode (from the data in Fig. 1d, in the main text). In DECP theory the oscillation phase is directly related to the lifetime of the driving force on the vibrational coordinate [1]. A value of 0 or 180 degrees indicates that the lifetime of the force is long compared to the period of the mode, whereas a value of  $\pm 90$  degrees indicates that the force lifetime is much smaller than the phonon period. Based on this, we can suppose that for the shear mode the driving force is indeed much smaller than the  $\approx 4$  ps mode period, whereas for the 2.4 THz mode the driving force may be more comparable to the  $\approx 400$  fs period. This last inference, whoever, must be interpreted with caution since small errors in the zero-time-delay can cause large changes in the value of the phase, and our estimates of zero time delay are derived from the fit to Eq. 1 (main text) and are somewhat correlated with the phase of the 2.4 THz mode.

The changes in the diffracted intensity at long time delays were investigated further for the ( $\bar{146}$ ), ( $\bar{162}$ ), ( $\bar{163}$ ) and (075) Bragg reflections. For pump-probe delays longer than a few picoseconds, there can be significant changes to the diffraction conditions due to the development of strain. In order to distinguish effects of strain from other changes in the structure factor of the reflections, we performed measurements of the total diffracted intensity  $I$  as a function of rotation about the sample normal  $\varphi$  for fixed values of the pump-probe delay. Pure strain (e.g. from thermal expansion) will cause only a shift of  $I(\varphi)$  [15] but leaves the integral with respect to  $\varphi$  unchanged. Changes in the structure factor, caused by either an increase in dynamic disorder (Debye-Waller factor) [3, 16] or a different arrangement of atomic positions in the average unit cell, will not affect the shape of the intensity profile  $I(\varphi)$  but do change the integrated intensity.

Supplementary Figures 18a-h show a summary of these data for the Bragg reflections we studied, with an absorbed pump fluence of  $3.2 \text{ mJ/cm}^2$ . Panels a, b, e and f report the equilibrium profiles, while c, d, g, h the differences between pumped and unpumped profiles. Here  $\Delta\varphi = 0$  is defined as the condition for optimal diffraction. At short time delays, we observe an overall modulation of the intensity with no change to the position or shape of the Bragg reflection. This is the expected behavior arising from the coherent optical phonons modeled in the main text, since these result in coherent changes in the relative position of atoms in an average unit cell, but do not alter the unit cell dimensions. After several tens of picoseconds, the differences between the pumped and equilibrium diffraction start to deviate from the equilibrium peak shape, indicating strain in addition to structure factor changes. From the time-dependent intensity measurements of Supplementary Figure 16b, these changes appear to plateau at times later than about 80 ps.

Interestingly, although the ( $\bar{163}$ ) Bragg reflection shows at 29 ps a clear decrease in integrated intensity, the ( $\bar{162}$ ) Bragg reflection at the same delay shows a marked increase in integrated diffraction, and the ( $\bar{146}$ ) and (075) peaks

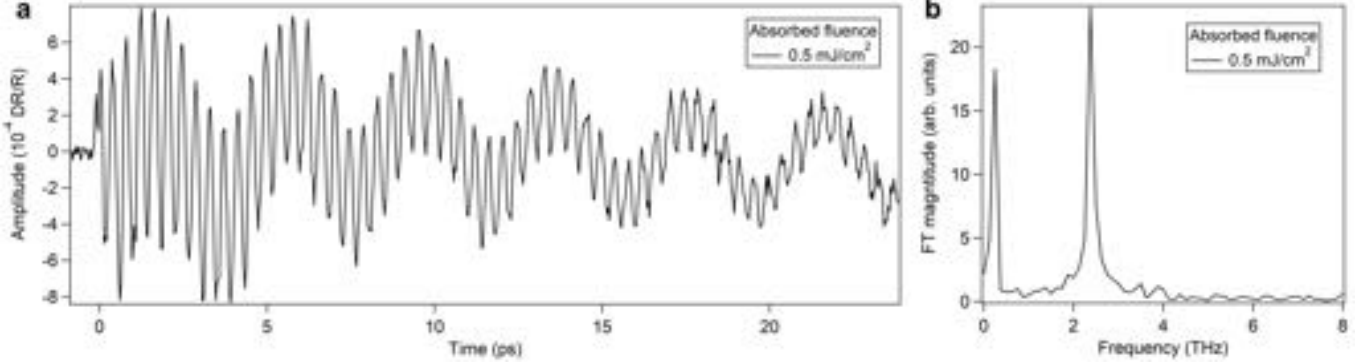
show very little change in their integrated intensity at the delay times of 29 and 100 ps respectively. These delays are already at times when the coherent oscillations are mostly damped out and so these differences are indicative of changes in the unit cell structure factor. Since dynamic disorder from an increased lattice temperature would result in a decrease in the integrated intensity for all peaks, it is clear from these data that there is a new quasi-equilibrium structure of the unit cell that is distinct from the initial equilibrium state. This can likely be explained by a change in the shear mode displacement, which would in fact result in contributions of opposite sign for the  $(\bar{1}63)$  relative to the  $(\bar{1}62)$ ,  $(\bar{1}62)$ ,  $(075)$  reflections (see Supplementary Figure 3 and the associated discussion in the last section). This is also supported by recent density-functional-theory / molecular dynamics simulations [4] and is compatible with a change of the structure towards the  $1T'(^*)$  structure proposed in Ref. [5], where the inversion symmetry, whose breaking allows the presence of non-trivial Weyl topology in the equilibrium structure [17], is present.



**Supplementary Figure 18. X-ray azimuthal scans.** Angular  $\varphi$ -scans without the pump excitation for the a ( $\bar{1}46$ ), b ( $\bar{1}62$ ), e ( $\bar{1}63$ ) and f (075) Bragg peaks normalized by the peak value.  $\Delta\varphi = 0$  is referred to the maximum intensity. The respective pump-induced variations are reported in panels c, d, g and h as percentage changes with respect to the intensity maximum measured without the near-infrared pump. The error bars represent one standard deviation uncertainty.

## SUPPLEMENTARY NOTE 4

In the analysis in the main text, we consider only two phonon modes to fit the near-infrared reflectivity data. This is justified by the results obtained from the Fourier transform (Supplementary Figure 19), where the 0.24 THz (shear mode) and 2.4 THz contributions dwarf the others at this probe wavelength.



**Supplementary Figure 19. Phonon modulation in the 950 nm reflectivity.** **a** Coherent oscillatory response from Fig. 4a, in the main text, after subtracting a decaying-exponential fit. **b** Fourier transform of the data in the 0-6 ps range from panel a acquired at room temperature and  $\approx 0.5 \text{ mJ/cm}^2$  absorbed fluence.

In the time-resolved reflectivity experiment (250 kHz repetition rate), we observed permanent reflectivity changes for absorbed fluences above  $9.1 \text{ mJ/cm}^2$ , which we did not detect under similar fluence conditions in the time-resolved x-ray diffraction data. The reason why we did not observe such modification during the x-ray experiment is likely connected to the much lower repetition rate (50 Hz) of the pumping system. Regarding the ‘onset’ fluence for this permanent process to reach a new equilibrium, we registered some variability ( $6.4\text{-}9.1 \text{ mJ/cm}^2$ ) depending on the portion of the crystal chosen.

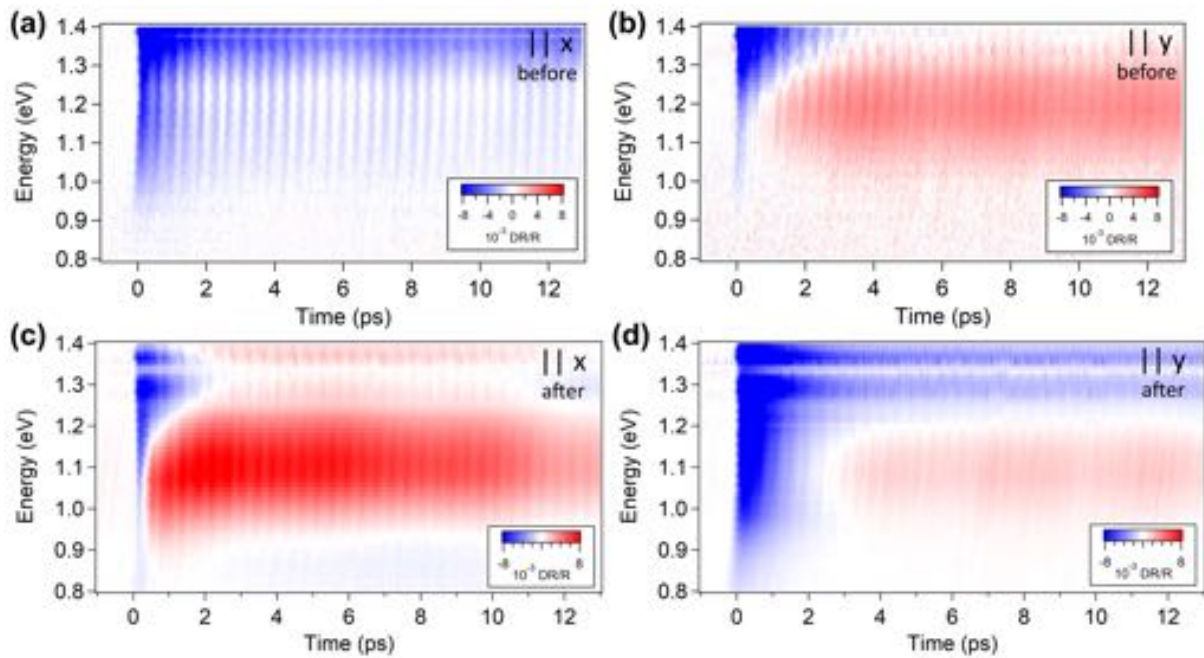
Looking at the reflectivity through a broadband probe after these permanent changes occur, we noticed that the response changed with a positive signal centered at 1.1 eV now present for both the polarizations, in contrast to the initial response (Supplementary Figure 20).

In order to better understand the reasons for the permanent sample changes at high fluence, we can roughly estimate the surface sample temperature assuming no transport effects over the time scales needed for thermalization [18]. This will overestimate the actual peak temperature, but nonetheless gives an indication of whether the melting temperature may be approached during the pump-probe cycle. The deposited heat is estimated as

$$Q_{\text{dep}} = Q_{\text{abs}} \rightarrow (1 - R)FA = \frac{Al_p\rho}{M_M} \int_{T_0}^{T_0+\Delta T} C(T)dT \rightarrow (1 - R)F = \frac{l_p\rho}{M_M} \int_{T_0}^{T_0+\Delta T} C(T)dT \quad (6)$$

where  $R$  is the reflectivity,  $F$  is the incident fluence,  $A$  is the excitation area,  $l_p$  is the intensity penetration depth,  $\rho$  is the mass density,  $M_M$  is the molar mass and  $C(T)$  is the temperature-dependent molar thermal capacity, whose data for  $\text{WTe}_2$  can be found in [19]. For the highest absorbed fluence the transient temperature increase of the lattice system becomes larger than the reported 1020-1300 K melting point [20, 21].

Despite this, the fact that the x-ray measurements do not show clear evidence of sample modifications suggests that transport effects are not negligible and so the variations seen in optical reflectivity are the result of time-average heating of the sample rather than significant permanent changes from individual shots. We nonetheless should consider that high transient temperatures comparable to the melting temperature are possible. This may explain the reduction of the shear mode amplitude seen at high fluences in Figs. 3c and 4c, in the main text, as the result of a large increase in phonon-phonon scattering at these temperatures. Moreover, the more isotropic response seen in Supplementary Figures 20c,d could be related to a deviation from the initial single-crystal morphology after the high-fluence exposure.



**Supplementary Figure 20. Broadband DR/R comparison.** **a,b** before the permanent change taken at  $\approx 0.7$   $\text{mJ}/\text{cm}^2$  absorbed fluence in [14] and **c,d** after the permanent change taken at  $\approx 0.5$   $\text{mJ}/\text{cm}^2$  using a 250 kHz laser system at room temperature. Data in panels a and c were acquired having the white probe polarized along the  $x$  crystallographic direction, while it was directed along  $y$  (see Supplementary Figure 6 for reference) for panels b and d; the pump beam, linearly polarized, was kept perpendicular to the probe.

SUPPLEMENTARY NOTE 5

Describing refraction at the interface between an isotropic medium like air and an absorbing biaxial system like  $\text{WTe}_2$  is more challenging than for an isotropic-isotropic case. In general, two transmitted beams have to be considered in the second medium, with distinct refraction angles and orthogonal polarizations [22]. In order to quantitatively describe the wave propagation, full knowledge of the dielectric tensor is required.

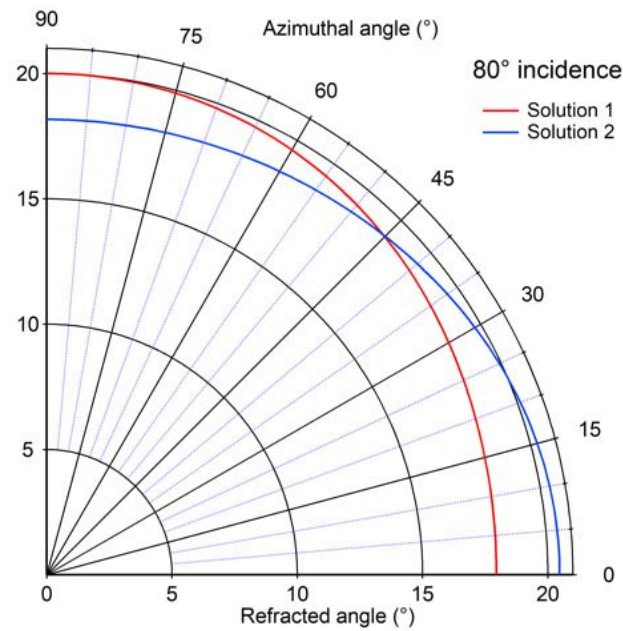
Due to the orthorhombic crystal system, the dielectric principal axes coincide with the crystallographic axes. Applying the boundary conditions for the electromagnetic field at the interface together with the frequency-wavevector dispersion relations in the two media [23], we derived the refraction angles. For this simulation, we exploited the diagonal dielectric tensor components in  $\text{WTe}_2$  as reported in [24], where a Tauc-Lorentz oscillator model was obtained starting from ellipsometry data. In our x-ray experiment, the near-infrared pulse arrived at the surface with a  $80^\circ$  angle with respect to the normal to the surface. In the reflectivity experiment, the near-infrared pump was set to be quasi-normal to the surface. We report the solutions for the first configuration in Supplementary Figure 21 as a function of the azimuthal angle.

Calculating the intensity penetration depth of the solutions, we noticed a large difference between the two, by almost a factor of four. This is linked to a marked in-plane anisotropy of the extinction coefficient derived using the Tauc-Lorentz oscillator model in [24]. Moreover, this translates into an anisotropy for the reflectivity of linearly polarized light along the two in-plane axes.

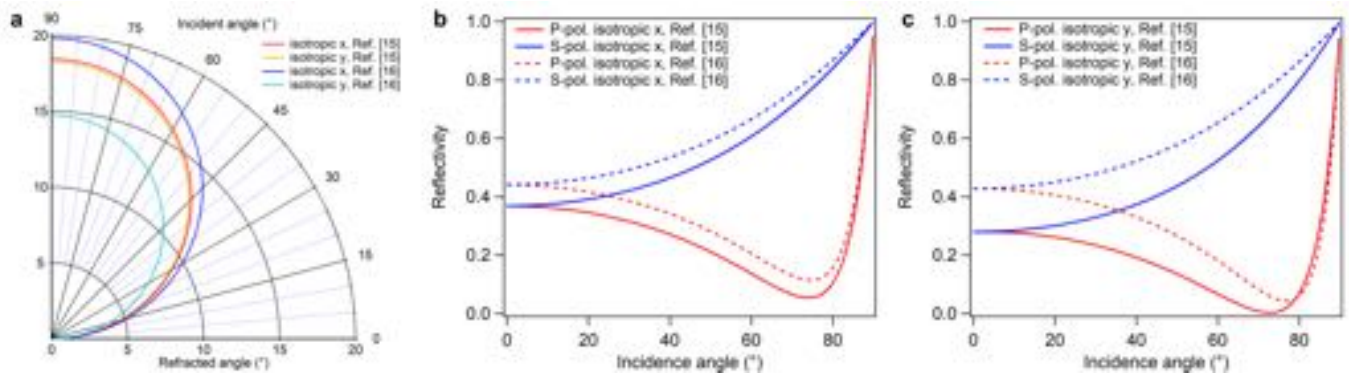
These characteristics are, however, in apparent contradiction with the data reported by Frenzel et al. [25] as well as with published data from some of the authors of this work on the specific samples under investigation [14]. Frenzel et al. found that the dielectric tensor for the in-plane axes leads to an almost isotropic response at 800 nm in terms of extinction coefficient ( $k$ ), intensity penetration depth and reflectivity (Supplementary Figure 23). These differences may derive from the crystals themselves, grown with different methods, but also from the different procedures used to obtain the values in the two referenced papers.

Since Frenzel et al. do not provide estimates of the  $zz$ -component of the dielectric tensor, it is not possible to fully solve for the double refraction using their optical constants. We instead calculate in Supplementary Figure 22 the refraction angles and reflection coefficients obtained by approximating the crystal as optically isotropic, with the value of the index of refraction set to each of its in-plane values. We do this using the in-plane constants from both references.

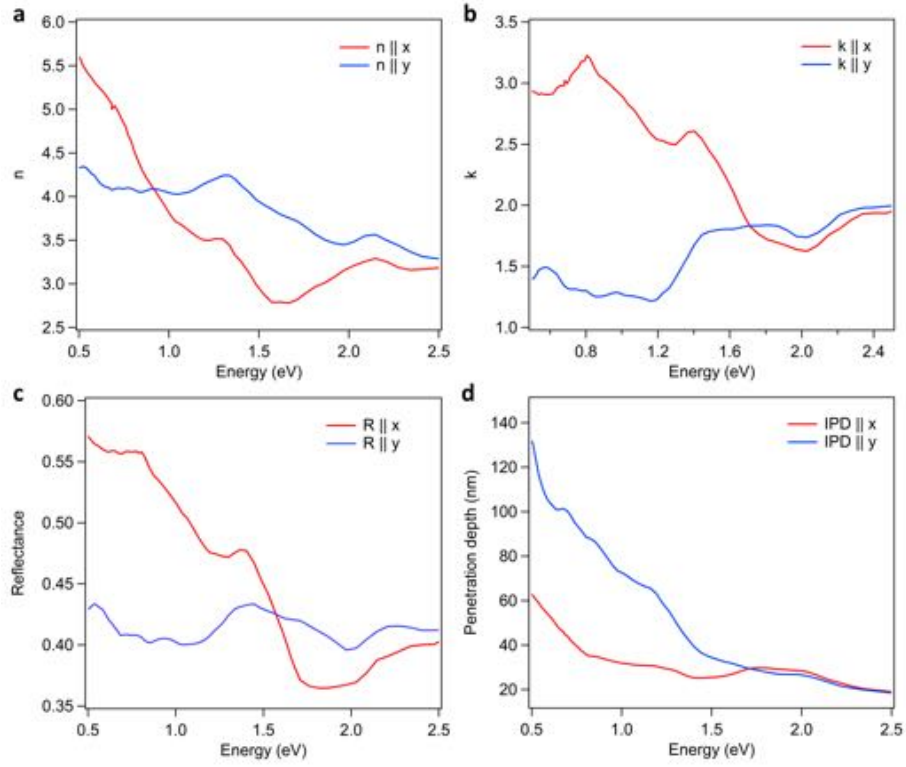
We note that regardless of how the optical anisotropy is treated, all calculations shown in Supplementary Figures 21 and 22 predict a refraction angle smaller than  $21^\circ$  for all beams. This justifies an approximation where we simply assume that the refracted beam has negligible out-of-plane polarization. The normal modes of the refracted beam then approximately correspond to the two in-plane polarizations. This implies that the reflectivity and attenuation length of the refracted beams are well-approximated by an isotropic model using the two in-plane principal axes. At  $80^\circ$  incidence varying the in-plane orientation of the sample results in a  $\pm 5.4\%$  uncertainty in reflectivity. At normal incidence (see Supplementary Figure 23) the variance in reflectivity with in-plane polarization results in a  $\pm 1.5\%$  uncertainty in the absorbed fluence. Due to the small refraction angle, in both cases the attenuation lengths are similar (see Supplementary Figure 23d) and show a maximum deviation of  $\pm 11\%$  of the attenuation length with sample rotation.



**Supplementary Figure 21. Refraction angles as a function of the azimuthal angle.** For the air-WTe<sub>2</sub> interface considering the anisotropic biaxial crystal and a 80° incidence angle, the azimuthal angular values are referred to the in-plane  $x$  direction while the refracted angles are referred to the  $z$  direction, normal to the interface. The solutions were calculated based on the data from Buchkov et al. [24].



**Supplementary Figure 22. Refraction and reflection in the isotropic approximation.** **a** Refraction angles as a function of the incident angles for the air-WTe<sub>2</sub> interface in the isotropic approximation taking alternatively the refractive indexes along the two in-plane crystallographic axes (more details in the text); the angular values are referred to the  $z$  direction, normal to the interface. **b,c** Dependence of the reflectance of WTe<sub>2</sub> in the same isotropic approximation. The angles are referred to the normal to the surface.



**Supplementary Figure 23. Anisotropic optical properties of  $\text{WTe}_2$ .** They were derived from the dielectric function data from Frenzel et al. [25] considering the electric field to be linearly polarized along the indicated direction. **a** Real and **b** imaginary parts of the refractive index; **c** normal-incidence reflectance **d** intensity penetration depth (considering normal incidence).

## SUPPLEMENTARY REFERENCES

- 
- \* e-mail:davideso@phys.ethz.ch  
 † e-mail:johnson@phys.ethz.ch
- [1] Zeiger, H. J. *et al.* Theory for dispersive excitation of coherent phonons. *Phys. Rev. B* **45**, 768–778 (1992).
  - [2] Mansart, B. *et al.* Temperature-dependent electron-phonon coupling in  $\text{La}_{2-x}\text{Sr}_x\text{CuO}_4$  probed by femtosecond x-ray diffraction. *Phys. Rev. B* **88**, 054507 (2013).
  - [3] James, R. W. *The optical principles of the diffraction of x-rays, The crystalline state - vol. II* (G. Bell & Sons, London, 1962).
  - [4] Guan, M.-X., Wang, E., You, P.-W., Sun, J.-T. & Meng, S. Manipulating Weyl quasiparticles by orbital-selective photoexcitation in  $\text{WTe}_2$ . *Nat. Commun.* **12**, 1885 (2021).
  - [5] Sie, E. J. *et al.* An ultrafast symmetry switch in a Weyl semimetal. *Nature* **565**, 61–66 (2019).
  - [6] Baroni, S., de Gironcoli, S., Dal Corso, A. & Giannozzi, P. Phonons and related crystal properties from density-functional perturbation theory. *Rev. Mod. Phys.* **73**, 515–562 (2001).
  - [7] Kokalj, A. XCrySDen—a new program for displaying crystalline structures and electron densities. *J. Mol. Graph. Model.* **17**, 176–179 (1999).
  - [8] Brown, B. E. The crystal structures of  $\text{WTe}_2$  and high-temperature  $\text{MoTe}_2$ . *Acta Crystallogr.* **20**, 268–274 (1966).
  - [9] Lassner, E. & Schubert, W.-D. *Tungsten, Properties, Chemistry, Technology of the Element, Alloys, and Chemical Compounds* (Springer US, New York, 1999).
  - [10] Takeda, T. The scalar relativistic approximation. *Z. Phys. B* **32**, 43–48 (1978).
  - [11] Giannozzi, P. *et al.* QUANTUM ESPRESSO: a modular and open-source software project for quantum simulations of materials. *J. Condens. Matter Phys.* **21**, 395502 (2009).
  - [12] Liechtenstein, A. I., Anisimov, V. I. & Zaanen, J. Density-functional theory and strong interactions: Orbital ordering in Mott-Hubbard insulators. *Phys. Rev. B* **52**, R5467–R5470 (1995).
  - [13] Di Sante, D. *et al.* Three-Dimensional Electronic Structure of the Type-II Weyl Semimetal  $\text{WTe}_2$ . *Phys. Rev. Lett.* **119**, 026403 (2017).
  - [14] Soranzio, D., Peressi, M., Cava, R. J., Parmigiani, F. & Cilento, F. Ultrafast broadband optical spectroscopy for quantifying subpicometric coherent atomic displacements in  $\text{WTe}_2$ . *Phys. Rev. Res.* **1**, 032033 (2019).
  - [15] Schlepütz, C. M., Mariager, S. O., Pauli, S. A., Feidenhans'l, R. & Willmott, P. R. Angle calculations for a (2+3)-type diffractometer: focus on area detectors. *J. Appl. Crystallogr.* **44**, 73–83 (2011).
  - [16] Ligges, M. *et al.* Observation of ultrafast lattice heating using time resolved electron diffraction. *Appl. Phys. Lett.* **94**, 101910 (2009).
  - [17] Soluyanov, A. A. *et al.* Type-II Weyl semimetals. *Nature* **527**, 495–498 (2015).
  - [18] He, B. *et al.* Coherent optical phonon oscillation and possible electronic softening in  $\text{WTe}_2$  crystals. *Sci. Rep.* **6**, 30487 (2016).
  - [19] Callanan, J. E., Hope, G., Weir, R. D. & Westrum, E. F. Thermodynamic properties of tungsten ditelluride ( $\text{WTe}_2$ ) I. The preparation and lowtemperature heat capacity at temperatures from 6 K to 326 K. *J. Chem. Thermodyn.* **24**, 627–638 (1992).
  - [20] Lide, D. R. *CRC Handbook of Chemistry and Physics, 85th Edition* (CRC Press, 2004).
  - [21] Tian, W., Yu, W., Liu, X., Wang, Y. & Shi, J. A Review of the Characteristics, Synthesis, and Thermodynamics of Type-II Weyl Semimetal  $\text{WTe}_2$ . *Materials* **11**, 1185 (2018).
  - [22] Born, M. & Wolf, E. *Principles of Optics: Electromagnetic Theory of Propagation, Interference and Diffraction of Light* (Cambridge University Press, 1999).
  - [23] Saleh, B. & Teich, M. *Fundamentals of Photonics* (Wiley, 2019).
  - [24] Buchkov, K. *et al.* Anisotropic Optical Response of  $\text{WTe}_2$  Single Crystals Studied by Ellipsometric Analysis. *Nanomaterials* **11** (2021).
  - [25] Frenzel, A. J. *et al.* Anisotropic electrodynamics of type-II Weyl semimetal candidate  $\text{WTe}_2$ . *Phys. Rev. B* **95**, 245140 (2017).